nature communications

Article

https://doi.org/10.1038/s41467-025-57129-6

Structural insights into S-lignin *O*-demethylation via a rare class of heme peroxygenase enzymes

Received: 17 July 2024

Accepted: 5 February 2025

Published online: 20 February 2025

Check for updates

Alix C. Harlington[1], Tuhin Das[2], Keith E. Shearwin[1], Stephen G. Bell[2] ✉ & Fiona Whelan[1,3] ✉

The *O*-demethylation of lignin aromatics is a rate-limiting step in their bioconversion to higher-value compounds. A recently discovered cytochrome P450, SyoA, demethylates the S-lignin aromatic syringol. In this work, we solve high-resolution X-ray crystal structures of substrate-free and substrate-bound SyoA and evaluate demethylation of *para*-substituted S-lignin aromatics via monooxygenase and peroxide shunt pathways. We find that SyoA demethylates S-lignin aromatics exclusively using the peroxide shunt pathway. The atomic-resolution structures reveal the position of non-canonical residues in the I-helix (Gln252, Glu253). Mutagenesis of this amide-acid pair in SyoA shows they are critical for catalytic activity. This work expands the enzymatic toolkit for improving the capacity to funnel lignin derived aromatics towards higher value compounds and defines the chemistry within the active site of the enzyme that enables peroxygenase activity. These insights provide a framework for engineering peroxygenase activity in other heme enzymes to generate easier to use biocatalysts.

Ubiquitous in all domains of life, the superfamily of heme-dependent cytochrome P450 enzymes (P450s) catalyze selective oxidations of unactivated C−H bonds. In recent years, P450s have gained traction as catalysts for lignin valorization—the process of converting the plant polymer lignin into commercially valuable chemicals[1]. The CYP255 family of P450s; so far consisting of GcoA[2], AgcA[3], and SyoA[4], catalyze the *O*-demethylation of lignin monoaromatics, which is an important step in the valorization of lignin. Lignin is a complex heterogeneous polymer comprising *p*-coumaryl (H-type), coniferyl (G-type) and sinapyl (S-type) alcohol subunits, which have zero, one or two methoxy groups, respectively[5] (Fig. 1a). Aromatics derived from lignin depolymerization must be *O*-demethylated to diols to permit formation of ring-opened compounds, which can be funnelled to high-value compounds, e.g., organic acids (*cis,cis*-muconate, pyruvate and lactate); pyridine-related organic acids (pyridine-2,4-dicarboxylic acid); and lipids which can be used to make various materials (polyamides and polyesters), fuels and flavors[6]. So far, three classes of enzymes have been identified that catalyze *O*-demethylation of S-lignin aromatics including: tetrahydrofolate (THF)-dependent demethylases[7,8], Rieske non-heme iron-dependent oxygenases[9,10], and P450s[4] (Fig. 1b). P450 enzymes have been engineered for improved demethylation of syringol, including GcoA[11] and CYP102A1 ($P450_{BM3}$)[12]; however, native enzymes capable of the *O*-demethylation of S-lignin aromatics remain largely undescribed.

Most P450s function as monooxygenases requiring redox partners to transfer two electrons to the heme iron from the nicotinamide cofactor NAD(P)H to activate dioxygen (O_2)[13,14]. Activation of dioxygen results in the formation of the oxy-ferryl porphyrin radical cation species compound I (Cpd I), the reactive intermediate[15,16] (Fig. 1c). In many P450s this process is mediated by two residues within the oxygen binding groove of the I-helix—referred to as the acid-alcohol

[1]Department of Molecular and Biomedical Science, University of Adelaide, Adelaide, SA, Australia. [2]Department of Chemistry, University of Adelaide, Adelaide, SA, Australia. [3]Adelaide Microscopy, University of Adelaide, Adelaide, SA, Australia. ✉e-mail: stephen.bell@adelaide.edu.au; fiona.whelan@adelaide.edu.au

https://doi.org/10.1038/s41467-025-57129-6

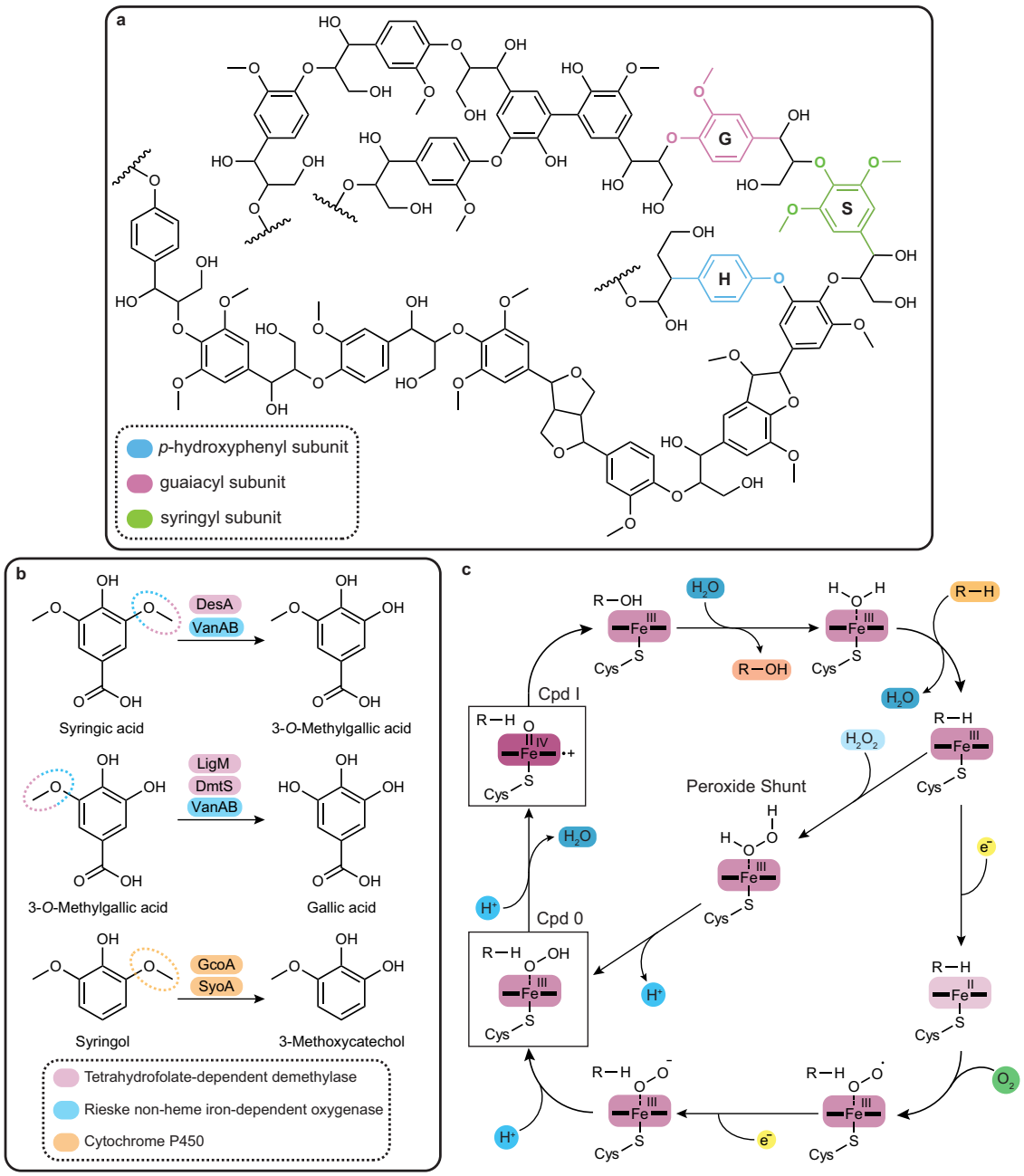

Fig. 1 | Lignin structure, S-lignin demethylases and P450 catalytic cycle. **a** Overall structure of lignin highlighting the main *p*-coumaryl (*p*-hydroxyphenyl, H-type, blue), coniferyl (guaiacyl, G-type, purple) and sinapyl (syringyl, S-type, green) alcohol subunits. **b** Schemes showing the *O*-demethylation reactions of S-lignin aromatics catalyzed by tetrahydrofolate-dependent demethylases DesA, LigM, and DmtS from *Sphingobium* sp. SYK-6 and *Novosphingobium aromaticivorans* DSM 12444 (pink), the Rieske non-heme iron-dependent oxygenase VanAB from *Pseudomonas putida* KT2440 (blue) and the cytochrome P450s SyoA and GcoA from *Amycolatopsis thermoflava* (orange). The target *O*-methyl groups for each enzyme are denoted by dashed circles colored by enzyme family. **c** Catalytic cycle of cytochrome P450s showing the monooxygenase pathway (outer circle) and the peroxide shunt pathway generating the transient intermediate hydroperoxo-ferric complex Compound 0 (Cpd 0), leading to formation of the reactive species Compound I (Cpd I). The oxidation state of Fe is indicated with a purple gradient; Fe^{II} light, Fe^{III} medium, and Fe^{IV}-oxo/porphyrin radical cation, dark purple.

pair (Asp/Glu-Thr/Ser). Specifically, the acid aids in the delivery of protons to the heme-oxygen intermediates, while the alcohol is believed to stabilize the ferric-hydroperoxo intermediate, compound 0 (Cpd 0) for efficient formation of Cpd I[17–21]. P450s can also use H_2O_2 to generate Cpd I by using the "peroxide shunt pathway", circumventing the need for additional redox partner proteins and expensive NAD(P)H cofactor (Fig. 1c)[22,23]. The majority of P450s are unable to use H_2O_2 efficiently, leading to heme destruction and enzyme inactivation[24]. However, some families of heme enzymes possess naturally high levels of peroxygenase activity and deploy residues capable of acid-base chemistry to activate H_2O_2. For example, the CYP152 family use the substrate's carboxyl group, coordinated to an Arg, to function as peroxygenases[25–27]. Furthermore, the P450 (*Ssca*CYP) was shown to hydroxylate *trans*-β-methyl-styrene and catalyze the sulfoxidation of thioanisole using H_2O_2[28]. Structural analysis of *Ssca*CYP revealed two acid-base residues in the active site; an Asp which replaces the canonical I-helix Thr, and a Glu near the K-helix. Other heme-containing peroxidases and peroxygenases also deploy residues capable of acid-base chemistry on the distal side of the heme[22,29]. It is believed that binding of H_2O_2 to the ferric form of these

https://doi.org/10.1038/s41467-025-57129-6

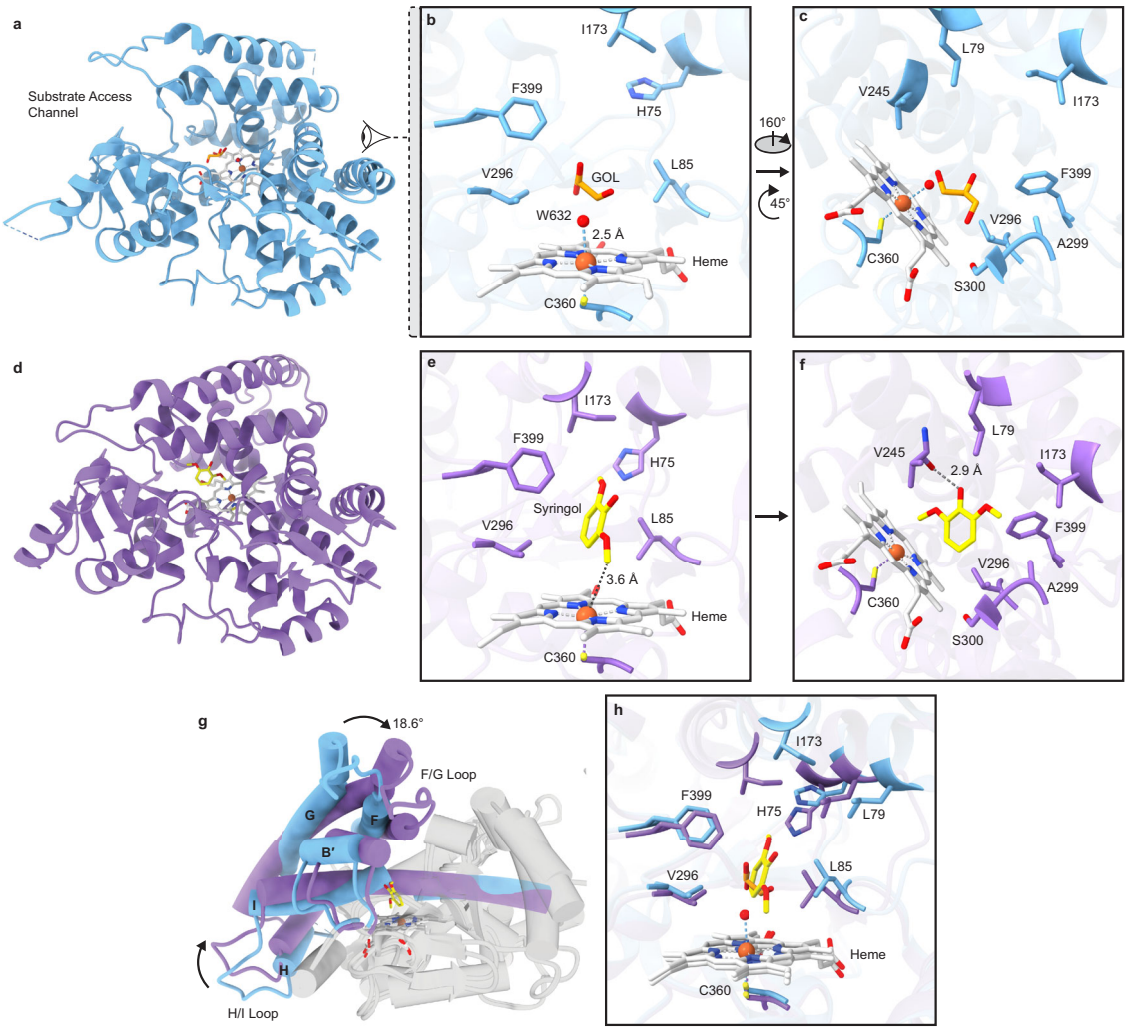

Fig. 2 | X-ray crystal structures of SyoA in the open substrate-free and closed substrate-bound states. Ribbon diagram showing the overall architecture of SyoA in the (**a**) open conformation (PDB: 8u09, blue) highlighting the positions of the heme (white sticks), sixth axial water (red sphere) and glycerol (GOL, orange/red sticks). **b**, **c** Active site of the open conformation showing the key active site residues highlighting the solvent molecules and Fe-OH_2 distance (blue dashed line). Ribbon diagram showing the overall architecture of SyoA in the (**d**) closed conformation (PDB: 8u19, purple) showing the positions of the heme (white) and substrate syringol (yellow/red). **e**, **f** Active site of the closed conformation highlighting key active site residues; black dashed lines illustrate the distance of the 2-methoxy group of syringol from the Fe center, and the hydrogen bonding distance between the 1-hydroxyl group of syringol and the backbone carbonyl of Val245. Superposed structures of the open and closed form of SyoA showing the **g** overall fold and **h** active site. Only the helices that have an average Cα RMSD of 3 Å or greater are colored in (**g**) with angle of displacement ~18.6° indicated by an arrow. The eye symbol (**b**) indicates the viewing angle of (**b**) relative to the structure shown in (**a**). The view of the active site in (**c**, **f**) is made by rotating (**b**, **e**) respectively ~160° clockwise about the *y*-axis, and ~45° clockwise about the *z*-axis.

enzymes results in deprotonation of the iron-bound oxygen, forming Cpd 0, with a protonation step resulting in O–O bond scission and dehydration leading to Cpd I (Fig. 1c).

Here we report high-resolution X-ray crystal structures of the recently identified CYP255 enzyme SyoA from *Amycolatopsis thermoflava* N1165 in the open substrate-free and closed substrate-bound states. These structures collectively reveal capacity in the active site to accommodate *O*-demethylation of *para*-substituted S-lignin aromatics. We demonstrate that SyoA functions more efficiently using the peroxide shunt pathway to demethylate S-lignin aromatics compared to the monooxygenase pathway. Additionally, we investigate the role of the amide-acid pair (QE) of residues, which sit above the heme within the I-helix, in the peroxygenase activity of the CYP255 enzymes SyoA and GcoA and monooxygenase activity of GcoA. Mutagenesis of the QE residues in SyoA and GcoA illustrates that, for this residue pair, both monooxygenase and peroxygenase activities are profoundly impacted by reversion to the canonical P450 ET sequence.

Results

Structural analysis and conformational change of SyoA

To investigate syringol binding by SyoA, we performed structural characterization by X-ray crystallography. Crystal structures of substrate-free (PDB: 8u09) and syringol-bound (PDB: 8u19) SyoA were determined at resolutions of 1.98 and 1.26 Å, respectively (Fig. 2, Supplementary Figs. 1, 2a–b, Supplementary Tables 1–4).

SyoA exhibits the characteristic single-domain trigonal prism shape, consisting of sixteen α-helices and four β-sheets, with the central heme iron coordinated by Cys360 (Fig. 2a, d, Supplementary Fig. 1). The substrate-free enzyme adopts an open conformation, with a water-filled channel that exposes the active site and heme to solvent (Fig. 2a–c, Supplementary Fig. 2a). The substrate access channel consists of a network of 13 hydrogen-bonded waters (Supplementary Fig. 3). On the distal side of the heme, an axial water is coordinated ~2.5 Å from the heme iron (Fig. 2b). Furthermore, unidentified electron density was observed in the active site that was too large for water and too small for syringol. The best candidate for the densities above the

https://doi.org/10.1038/s41467-025-57129-6

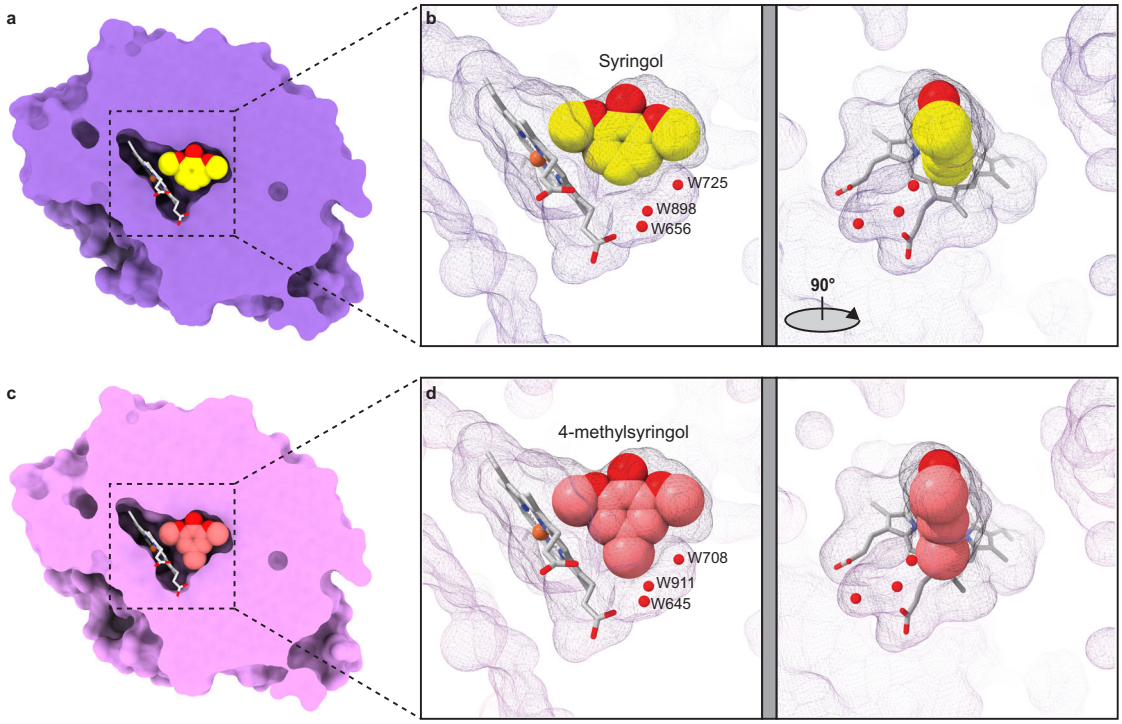

Fig. 3 | Comparison of active site volumes in the closed substrate-bound state. Surface rendering of **a** a slab view of the active site of SyoA (purple) bound to syringol (yellow/red large spheres) and **b** wireframe surface of the active site pocket showing the position of the heme (white sticks), syringol (yellow/red) and waters (small red spheres) that occupy the pocket. Surface rendering of **c** a slab view of the active site of SyoA (pink) bound to 4-methylsyringol (light red/red large spheres) and **d** wireframe surface of the active site pocket showing the heme (white sticks), 4-methylsyringol (light red/red) and waters (small red spheres). Surface renders (**a**, **c**) are clipped through the center of SyoA at the position of the substrate. The second image (**b**, **d**) is rotated 90° clockwise about the *y*-axis relative to the first pane.

heme and Phe399 was glycerol from the cryoprotectant, while density near His75 was consistent with acetate present in the crystallization conditions (Supplementary Fig. 3).

In contrast, the syringol-bound structure of SyoA adopts a closed conformation with the heme and substrate buried within a closed active site (Fig. 2d, Supplementary Fig. 2b). The active site of SyoA is predominantly hydrophobic, consisting of His75, Leu79, Leu85, Ile173, Val245, Val296, Ala299, Ser300, and Phe399 (Fig. 2e, f). Syringol is situated in the active site, with one methoxy carbon positioned towards the heme ~3.6 Å from the iron, and the other methoxy group positioned adjacent to His75 and Ile173 (Fig. 2e). Moreover, the aromatic ring of syringol is held between Leu85 and Phe399 with the hydroxyl group of syringol hydrogen-bonded to the carbonyl of Val245 (Fig. 2e–f). The network of water molecules observed in the substrate-free structure are not present in the substrate-bound form.

The conformational change between the open and closed state of SyoA is characterized by an ~19° displacement of helices B′, F, G, and H; and the F/G and H/I loops, via a hinge-like mechanism (Fig. 2g, Supplementary Fig. 4a and Supplementary Table 2). Displacements are observed for residues His75 (2.5 Å) and Leu79 (2.6 Å) of the B′-helix and Ile173 (4.4 Å) of the F-helix, which directly interact with one of the methoxy moieties of syringol (Fig. 2h, Supplementary Table 3). The G/H-loop, comprising residues 206–221, was not modeled in the open conformation due to poor resolution of the electron density. The average *B*-factors were highest surrounding the G/H-loop and were significantly lower in the closed state, consistent with stabilization of this region upon substrate binding (Supplementary Fig. 4b). Clear electron density was observed in the closed conformation enabling building and refinement of the G/H-loop in the bound state.

The closest structural homolog to SyoA is GcoA (PDB: 5ncb)[2]; the aligned structures reveal that relative to GcoA, there is additional space in the active site of SyoA, consistent with SyoA being permissive of binding to S-lignin aromatics which contain an additional methoxy group compared to G-lignin aromatics (Supplementary Figs. 5, 6). A triad of phenylalanine residues (Phe75, Phe169, and Phe395) is critical in positioning the aromatic ring of guaiacol in the active site of GcoA[2]. SyoA does not contain this triad of phenylalanine residues; instead, Leu79, Ile173 and Phe399 occupy equivalent positions in the active site (Supplementary Fig. 6a, b). Unique to the active site of SyoA is His75 (the equivalent residue in GcoA is Gly71), which partially fills the void in the active site occupied by larger aromatic residues in GcoA (Supplementary Fig. 6a).

Active site binding of *para*-substituted S-lignin aromatics

Substrate binding to P450s commonly induces a shift from a low to high-spin (HS) ferric state. The low-spin (LS) state is characterized by heme coordination of 6 ligands (Soret maximum at ~419 nm), including the active site water; the transition to a HS state (Soret maximum at ~390 nm) occurs when the substrate displaces this water. Previously, our analysis showed that SyoA preferentially binds syringol (**1**) over guaiacol[4]. The high-resolution crystal structure of syringol-bound SyoA reveals additional space in the active site at the substrate C4 carbon – *para* to the hydroxyl group of syringol (Fig. 3a, b). Consequently, we investigated binding of *para*-substituted S-lignin aromatics to SyoA including 4-methylsyringol (**2**), syringaldehyde (**3**), syringic acid (**4**), acetosyringone (**5**), 4-allylsyringol (**6**), sinapic acid (**7**) and sinapyl alcohol (**8**) (Fig. 4a). Strong absorbance of syringaldehyde, acetosyringone and sinapic acid in the visible spectrum from 420–390 nm made it difficult to investigate binding using the Soret band: therefore, the Q-bands at 568 and 535 nm were used to interrogate binding. Among the tested S-type aromatics, four demonstrated binding to SyoA with syringol

https://doi.org/10.1038/s41467-025-57129-6

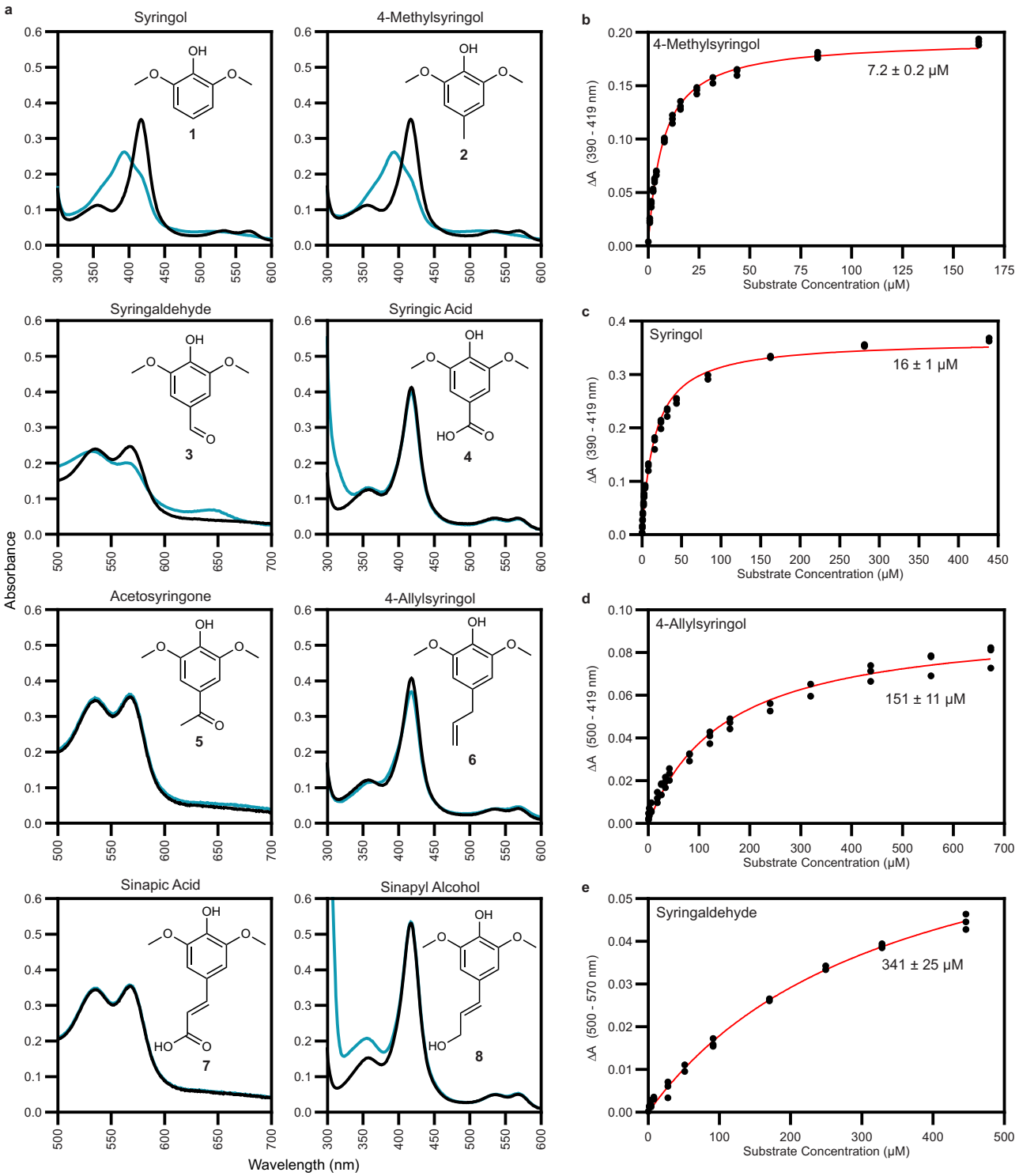

Fig. 4 | Binding analysis of S-lignin aromatics to SyoA. a In vitro spin-state shifts showing changes in the Soret peak (417 nm) for syringol, 4-methylsyringol, syringic acid, 4-allylsyringol and sinapyl alcohol or Q-bands (568 and 535 nm) for syringaldehyde, acetosyringone, and sinapic acid before (black) and after (blue) addition of each ligand. Each ligand was titrated into a solution containing SyoA and the UV-Vis absorbance spectrum monitored until the Soret band or Q-bands stopped shifting. Binding affinity curves of **b** 4-methylsyringol, **c** syringol, **d** 4-allylsyringol and **e** syringaldehyde to SyoA. Replicates $n = 3$ from distinct samples, with individual measurements shown as black dots.

and 4-methylsyringol inducing a ~70% shift to the HS form and 4-allylsyringol a ~15% shift using the Soret band (Fig. 4a). Addition of syringaldehyde to SyoA caused a decrease in the Q-bands, and an increase in the charge transfer band at ~640 nm indicative of ligand binding in the active site (Fig. 4a and Supplementary Fig. 7a). Binding analysis showed that SyoA binds 4-methylsyringol with the highest affinity ($K_D = 7.2 \pm 0.2\,\mu M$), followed by syringol ($K_D = 16 \pm 1\,\mu M$), 4-allylsyringol ($K_D = 151 \pm 11\,\mu M$) and syringaldehyde ($K_D = 341 \pm 25\,\mu M$) (Fig. 4b–e and Supplementary Fig. 7a–d).

Crystallization of SyoA was subsequently conducted with the addition of 4-methylsyringol. The atomic-resolution crystal structure of SyoA bound to 4-methylsyringol (PDB: 8u1i) was solved at 1.12 Å; no

https://doi.org/10.1038/s41467-025-57129-6

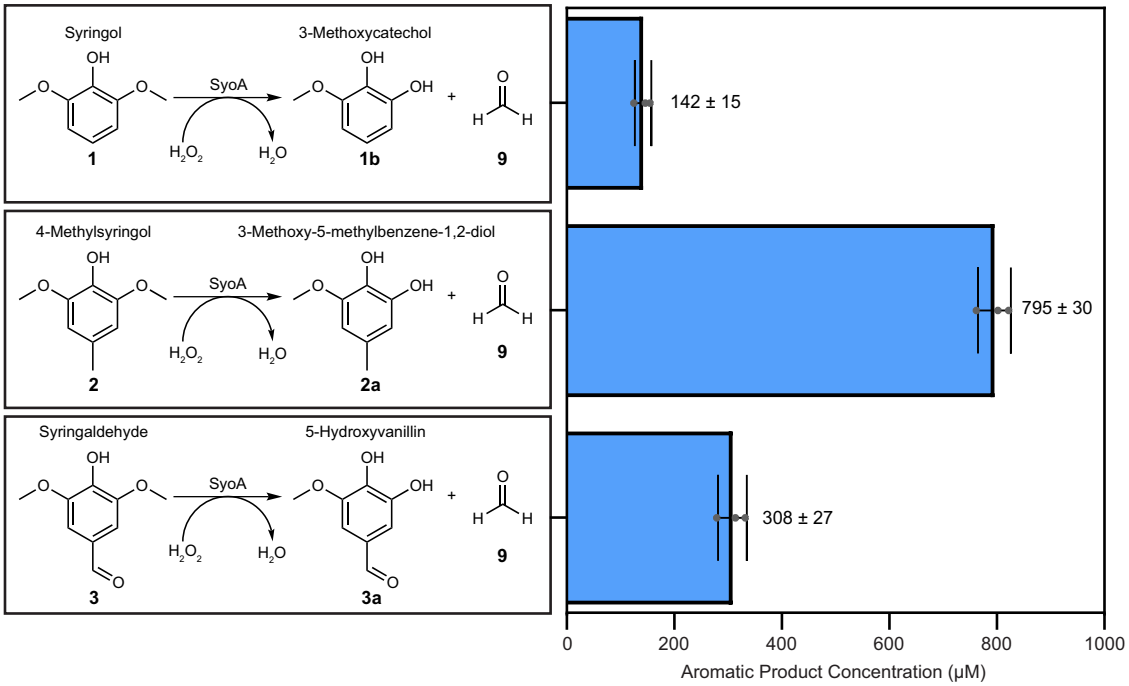

Fig. 5 | *O*-demethylation of S-lignin aromatics by SyoA using the peroxide shunt. Schemes showing the major products produced during the *O*-demethylation of syringol, 4-methylsyringol and syringaldehyde by SyoA. Reactions were carried out using 1 μM SyoA in 50 mM Tris pH 7.5, 10 mM H_2O_2; and 0.5 mM syringol, 0.5 mM syringaldehyde or 2 mM 4-methylsyringol at 30 °C for 60 min prior to quenching with catalase. Products were analyzed and the total concentration of the demethylated aromatic product measured. Error bars indicate ± 1 standard deviation from the mean of 3 replicates (black dots) from distinct samples including: 3-methoxycatechol 155, 125, 146 μM; 3-methoxy-5-methylbenzene-1,2-diol 802, 822, 762 μM; and 5-hydroxyvanillin 332, 314, 279 μM.

significant differences were observed in the active site, nor in the position of the substrate, with an all-atom RMSD of 0.35 Å between the syringol and 4-methylsyringol-bound structures (Fig. 3c, d, Supplementary Figs. 2c, 8 and Supplementary Table 1). The 4-methyl group occupies the vacant space observed in the syringol-bound structure, with the remaining space occupied by three water molecules which are conserved in both structures (Fig. 3c, d).

SyoA *O*-demethylates S-lignin aromatics using hydrogen peroxide

The CYP255 members GcoA and AgcA catalyze the *O*-demethylation of G-lignin aromatics, as a two-component system, using their respective three-domain redox partners (GcoB and AgcB). To determine the catalytic range of SyoA, we first investigated the *O*-demethylation of S-lignin aromatics using the monooxygenase pathway with the predicted redox partner SyoB, the encoding gene being adjacent SyoA (Supplementary Fig. 9). In contrast to GcoB and AgcB, SyoB consists of a predicted N-terminal FMN binding domain, NADH binding domain and a 2Fe-2S ferredoxin domain making it more structurally similar to the phthalate dioxygenase reductase family[30]. Unlike the other CYP255 members, the reconstituted SyoA/SyoB monooxygenase system did not *O*-demethylate syringol, 4-methylsyringol, or syringaldehyde (Supplementary Figs. 10, 11). However, NADH was consumed in the reaction containing SyoA, SyoB and syringol (Supplementary Fig. 10a–c). HPLC analysis identified 2,6-dimethoxyhydroxyquinone (**1a**) as the major product which, importantly, was also observed in the negative control excluding SyoA. This result indicates that syringol is reduced by SyoB in the presence of NADH, leading to uncoupling of electron transfer from SyoA (Supplementary Fig. 10d).

We next investigated the *O*-demethylation of syringol, 4-methylsyringol, syringaldehyde and 4-allylsyringol using the peroxide shunt pathway. Reactions with syringol, 4-methylsyringol and syringaldehyde all yielded demethylated products (catechols) and formaldehyde (**9**) as a by-product (Fig. 5, Supplementary Fig. 12). We observed no evidence that SyoA could do two successive demethylation reactions to produce pyrogallols. Additionally, several other products (due to overoxidation of the catechols by excess hydrogen peroxide) were observed in each reaction. The *O*-demethylation of syringol (**1**) yielded 142 ± 15 μM (total turnover number (TTN) 142) 3-methoxycatechol (**1b**), with ~65% of the substrate consumed over 60 min (Fig. 5, Supplementary Figs. 13, 17a). The demethylation of 4-methylsyringol (**2**) occurred to the greatest degree, with 795 ± 30 μM (total turnover number (TTN) 795) 3-methoxy-5-methylbenzene-1,2-diol (**2a**) produced over the 60 min reaction (Fig. 5, Supplementary Figs. 14, 17b). Syringaldehyde was demethylated to 5-hydroxyvanillin (**3a**) (308 ± 27 μM, TTN 308) (Fig. 5, Supplementary Fig. 15a). The reaction with syringaldehyde also liberated 2,6-dimethoxyhydroxyquinone (**1a**) / 2,6-dimethoxy-1,4-benzoquinone (**3c**) and 1,3,4-trihydroxy-5-methoxybenzene (**3b**) due to oxidation of the aldehydes by hydrogen peroxide via a Dakin oxidation reaction[31] (Supplementary Figs. 15b, c, 17c, 18). The oxidation of 4-allylsyringol (**6**) by SyoA yielded several metabolites in low yield as observed by HPLC, with one of the products confirmed to be 4-allylsyringol +[O] (m/z = 210) (Supplementary Figs. 16, 17d).

Structure and mutagenesis of the I-helix catalytic residues

The I-helix of P450 enzymes contains residues important for oxygen activation and catalysis[32]. We previously identified that the I-helix of the CYP255 family does not have the conserved acid-alcohol pair believed to be responsible for the monooxygenase function of most P450 enzymes[4]. The crystal structures of SyoA and GcoA reveal that the glutamine-glutamate pair (Gln252 and Glu253 SyoA; Gln248 and Glu249 GcoA) are observed in a structurally equivalent position to the acid-alcohol residues of most P450 enzymes and are likely to be important for the peroxygenase activity of the CYP255 family (Fig. 6a–c).

In the substrate-free state of SyoA, the I-helix exhibits a break in the α-helical structure from Gly249 to Gln252 due to the backbone amide of Glu253 forming a hydrogen bond with the carbonyl oxygen of

https://doi.org/10.1038/s41467-025-57129-6

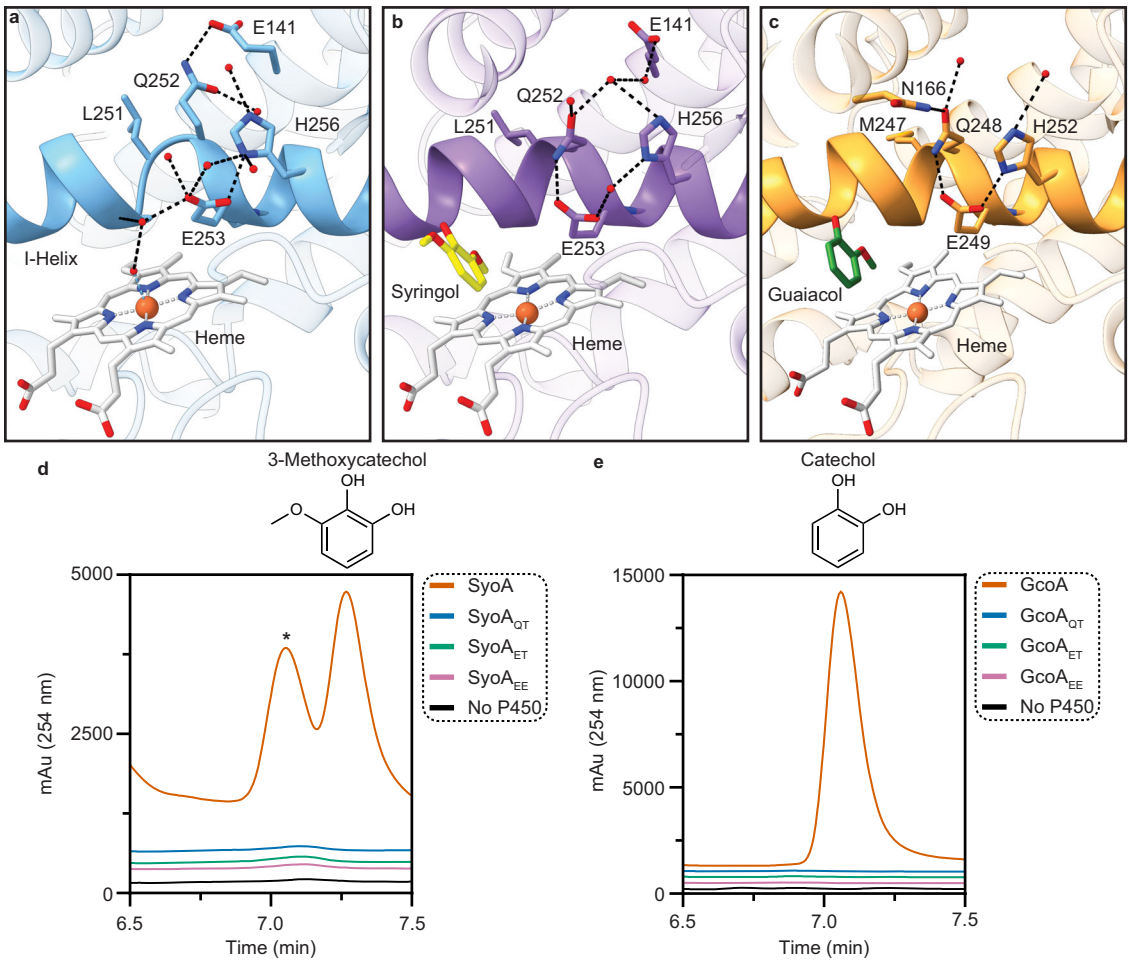

Fig. 6 | Mutagenesis of the I-helix catalytic residues. Ribbon and stick diagrams showing the I-helix of **a** SyoA substrate-free (PDB: 8u09), **b** SyoA syringol-bound (PDB: 8u19), and **c** GcoA guaiacol-bound (PDB: 5ncb). The I-helix is highlighted showing the key catalytic residues Gln252/Gln248 and Glu253/Glu249 (stick representation) and hydrogen bonding interactions (black dashed lines) to surrounding residues and water molecules (small red spheres). **d**, **e** HPLC analysis of the hydrogen peroxide driven *O*-demethylation of syringol by SyoA and guaiacol by GcoA compared to the mutants; chromatogram colors are defined in the key. Despite being folded, and competent for substrate binding, mutation of Gln and/or Glu resulted in loss of peroxygenase activity in both SyoA and GcoA. *Denotes non-enzymatic oxidation product of 3-methoxycatechol.

Gly250 (Fig. 6a). In the syringol-bound complex, the break is resolved due to the backbone amide of Glu253 forming a hydrogen-bond with the carbonyl of Gly249 instead (Fig. 6b). This conformational change affects the position of the glutamine–glutamate pair. In the substrate-free structure Gln252 is hydrogen-bonded to Glu141 of the E-helix, while Glu253 forms several interactions with surrounding solvent molecules and His256 (Fig. 6a). Upon substrate binding, Gln252 forms a hydrogen bond to Glu253, moving closer to the heme (Fig. 6b). Additionally, the direct hydrogen bond between Glu253 and His256 is disrupted by a water molecule. The I-helix of GcoA (PDB: 5ncb) adopts a similar conformation to SyoA, however, Gln248 hydrogen bonds to Asn188 of the F-helix and Glu249 directly interacts with His252 (Fig. 6c). In the substrate-bound structures the glutamic acid is located ~7.4 Å (SyoA) or ~8.1 Å (GcoA) from the heme iron and ~6.0 Å (SyoA) or ~6.8 Å (GcoA) from the 2-methoxy carbon.

To determine whether the non-canonical I-helix residues of the CYP255 family are important for peroxygenase activity, we performed site-directed mutagenesis on SyoA (Gln252 and Glu253) and GcoA (Gln248 and Glu249). We investigated double mutants (SyoA$_{ET}$ and GcoA$_{ET}$), where the QE residues were replaced with those commonly found in typical P450 monooxygenases. Additionally, to assess the specific contribution of each individual residue to catalytic activity, we also created single mutants (SyoA$_{EE}$/GcoA$_{EE}$ and SyoA$_{QT}$/GcoA$_{QT}$). UV-Vis analysis demonstrated that binding of syringol to SyoA and guaiacol to GcoA was not drastically impacted by the mutations, indicating that changes in catalytic activity are not likely due to loss of substrate binding (Supplementary Fig. 19a–b). Mutation of either the glutamine or glutamate in SyoA and GcoA was sufficient to completely remove catalytic function using the peroxide shunt (Fig. 6d–e). Furthermore, we also investigated the impact of the mutations on the monooxygenase activity of GcoA, which showed a significant reduction in the monooxygenase activity for GcoA$_{EE}$ and GcoA$_{ET}$ and complete loss in activity for the GcoA$_{QT}$ mutant (Supplementary Fig. 20).

Discussion

In contrast to chemical catalytic approaches, the *O*-demethylation of lignin aromatics using biocatalysis is of great interest as it offers an environmentally friendly method for converting lignin to high-value compounds[33,34]. Few S-lignin specific *O*-demethylases have been characterized, limiting the bioconversion of lignin from hardwoods and grasses. In this study, we determined the X-ray crystal structures of CYP255 SyoA in the open substrate-free and closed substrate-bound states and show that, in vitro, SyoA only catalyzes *O*-demethylation using the peroxide shunt pathway.

Compared to GcoA, SyoA has additional space in the active site allowing for binding of larger S-lignin aromatics. Specifically, SyoA

contains an isoleucine (Ile173) at the equivalent position of a key phenylalanine residue (Phe169) present on the F-helix, which has been shown to prevent productive binding of syringol in GcoA due to a steric clash with the second methoxy group[11]. Mutagenesis of this residue in GcoA to an alanine increases specificity for syringol[11] demonstrating that Ile173 in SyoA and Phe169 in GcoA may be responsible for determining specificity between S-lignin and G-lignin aromatics, respectively. Compared to GcoA, the active site of SyoA contains additional space at the *para* position allowing for binding of *para*-substituted aromatics (4-methylsyringol, syringaldehyde and 4-allylsyringol), due to the presence of an active site serine (equivalent position in GcoA features a threonine). Syringaldehyde is a major product of oxidative lignin depolymerization[35,36], while syringol and 4-methylsyringol are more commonly observed during lignin pyrolysis[36,37], making SyoA a suitable catalyst for aromatics derived from different methods of lignin depolymerization.

Various P450 enzymes are known to undergo conformational changes from open to closed states upon substrate binding[38]. In this work, we provide structural evidence that SyoA switches from an open to closed conformation in the presence of substrate, with relocation of the F, G and B′ helices to establish the closed hydrophobic active site of SyoA. The results described here support molecular dynamics (MD) simulations that show closing of the active site of GcoA in response to substrate binding[2]. Contrary to these observations, MD simulations predict AgcA (CYP255A1) prefers a closed conformation with smaller substrates but adopts an open conformation with larger substrates[39].

Like most P450 monooxygenase enzymes, GcoA and AgcA catalyze substrate oxidation using their respective redox partners, NAD(P)H and O_2. Interestingly, SyoA with its predicted redox partner SyoB demonstrated no *O*-demethylation of syringol, 4-methylsyringol and syringaldehyde. However, low levels of SyoB-dependent oxidation of syringol to 2,6-dimethoxyhydroxyquinone was observed. The presence of redox-active quinones can result in NADH oxidation, transferring the electrons via the redox partners to the quinone. This results in uncoupling of electron transfer from the P450 activity, explaining the oxidation of NADH without product formation[40]. This phenomenon has also been observed for VanB and syringic acid[10] indicating that some lignin aromatics may lead to uncoupling via redox cycling. However, SyoA and GcoA can efficiently use the peroxide shunt pathway to catalyze *O*-demethylation of their substrates—an uncommon feature of P450s[4]. Using the peroxygenase activity of SyoA, we were able to show *O*-demethylation of syringol, 4-methylsyringol and syringaldehyde. To our knowledge this is the first report of an enzyme that can demethylate the S-lignin aromatics 4-methylsyringol and syringaldehyde—which present as key bottlenecks to biological lignin valorization.

SyoA stands out among lignin-degrading enzymes for its ability to catalyze the *O*-demethylation of S-lignin aromatics using H_2O_2, a feature more common with certain heme-containing peroxidases than with other enzyme classes. Laccases, for instance, utilize O_2 to perform indirect C-C bond cleavage in lignins by generating mediators, such as phenoxy radicals, which facilitate further degradation[6,41]. In contrast, heme-containing peroxidases, including manganese peroxidases, lignin peroxidases, versatile peroxidases, and dye-decolorizing peroxidases, employ H_2O_2 to directly cleave C-C bonds in lignin structures[41]. Compared to hydroxylases, decarboxylases, and dioxygenases—which commonly use O_2 for their catalytic activity—the CYP255 family, including SyoA, is distinct in its efficient use of H_2O_2, thereby simplifying the catalytic requirements[42].

High-resolution structural analysis of the I-helix of SyoA has revealed the conserved acid-alcohol pair—typically found in P450 monooxygenases—is replaced with an amine-acid pair (glutamine and glutamate). Interestingly, peroxidases and peroxygenases contain amino acids capable of acid-base chemistry (histidine, aspartate, or glutamate) on the distal side of the heme[22,29]. We performed site-directed mutagenesis on the amine-acid pair of SyoA and GcoA and demonstrated the importance of the non-canonical I-helix residues for both the monooxygenase and peroxygenase function. All mutants lost the ability to use the peroxide shunt pathway with significant reduction in the monooxygenase activity also observed for GcoA, demonstrating the amide-acid pair is important for both oxygen and hydrogen peroxide activation in the CYP255 family.

We postulate that the CYP255 family may have evolved hybrid monooxygenase/peroxygenase enzyme activity for several reasons. Phylogenetic analysis of the CYP255 family compared to other P450 families shows that the peroxygenase activity may have evolved from a common ancestor to the CYP255 and CYP1232 family – both of which demethylate aromatics (Supplementary Fig. 21). Additionally, the peroxygenase activity appears to have evolved separately compared to other P450 peroxygenases including the CYP152 and SscaCYP (CYP177), indicating unique selection pressures. As shown by the reaction of syringol with SyoB, CYP255 enzymes may have evolved peroxygenase activity to avoid uncoupling via redox cycling by quinones. Hydroquinones including 2-methoxyhydroquinone ($MBQH_2$) and 2,6-dimethoxyhydroxyquinone ($DBQH_2$) can be derived from products of lignin degradation[43,44]. Furthermore, exposing lignin to light facilitates production of hydrogen peroxide[45,46]. Interestingly, many enzymes involved in the depolymerization of lignin also use H_2O_2 as a cosubstrate, suggesting these peroxygenases may have evolved to use hydrogen peroxide as a 'free' catalytic driver, removing the reactive oxygen species and thereby protecting the P450 from oxidative stress[47]. Thus, the CYP255 family may have evolved hybrid monooxygenase/peroxygenase enzyme activity as a mechanism to minimize uncoupling in the presence of quinones, using the hydrogen peroxide generated to drive catalysis.

The biochemical and structural data presented here suggest that SyoA is involved in the *O*-demethylation of S-lignin aromatics, which could allow *Amycolatopsis thermoflava* to funnel lignin monoaromatics to central carbon metabolism. Demethylation of syringol, 4-methylsyringol and syringaldehyde liberate catechols which other enzymes could further catabolize as an energy source to facilitate efficient lignin breakdown. Moreover, the atomic resolution structural insights also offer scope for engineering the active site of SyoA to accommodate other S-lignin aromatic substrates, including syringic acid or 3-*O*-methylgallic acid, expanding its utility. Additionally, the peroxygenase activity of the CYP255 family offers an inexpensive and clean approach to demethylation compared to traditional monooxygenases, which require specific redox partners and expensive nicotinamide cofactors. Using the sequence of the I-helix and surrounding regions of the CYP255 family may enable the retrofitting of peroxygenase activity into other P450s, making biocatalysis more favorable for larger scale applications. Indeed, the weak peroxygenase activity of CYP119[48] and CYP199, CYP154C8, and CYP102[49] was improved by mutating the acid-alcohol pair and surrounding residues to resemble the I-helix of the CYP255 enzymes.

Methods

General

Chemical reagents were purchased from Sigma-Aldrich. HPLC grade solvents were from Sigma-Aldrich, Ajax Finechem, and Chem-Supply. Enzymes, biochemical and molecular biology reagents were supplied by Sigma-Aldrich, New England Biolabs, and Thermo Fisher Scientific. Crystallography reagents, MicroMounts, MicroLoops, and MicroTools were from Hampton Research and Molecular Dimensions and the NVH oil from (Cargille Laboratories). Substrate and product stocks were prepared in DMSO. IS (internal standard) stock solutions were prepared in EtOH.

Gene cloning

A pET3a vector containing a codon optimized gene encoding SyoA was obtained using Gibson isothermal assembly[50], by 3-fragment assembly

with a single polymerase chain reaction (PCR)-generated insert fragment containing the *syoA* gene and two plasmid backbone fragments. The *syoA* gene was PCR amplified from the pET29-*SyoA* vector[4] using primers 3558 and 3559 (Supplementary Tables 5 and 6). The pET3a backbone fragments were PCR-generated using primers pairs 2281 and 3312 and 3497 and 1330 (Supplementary Table 6). SyoA mutants were made by 2-fragment Gibson assembly using the pET3a SyoA vector as the template. Primers 679 and 3991 were used to generate the first fragment and primer 1330 paired with 3992, 3993, or 3994 were used to generate the mutants $SyoA_{QT}$, $SyoA_{EE}$, $SyoA_{ET}$, respectively. Primers 215 and 315 (T7 promoter and T7 terminator, respectively) were used to sequence the insert fragment (Australian Genome Research Facility, Adelaide, Australia). A pET26-*GcoA* vector[4] was used for bacterial expression of GcoA. GcoA mutants ($GcoA_{EE}$, $GcoA_{QT}$, $GcoA_{ET}$) were purchased (Twist Bioscience) cloned in the pET28a plasmid with an N-terminal 6x His tag and Tobacco etch virus (TEV) cleavage site followed by a *Nde*I restriction site and the sequence for the gene of interest. Codon optimized genes encoding SyoB (based on the NCBI reference sequence: WP_027930991) and GcoB were purchased as gBlocks from IDT. An *Nde*I restriction site was incorporated at the 5′ end, followed by a double stop codon and *Kpn*I and *Hind*III restriction sites. PCR was performed on the gBlock DNA using primers RS0114865 5′ and RS0114865 His 3′ for SyoB and RS0109265 5′ and RS0109265 His 3′ for GcoB to add a 6x His tag to the C-terminus of the gene and inserted into a pET29b vector using the *Nde*I and *Hind*III restriction sites. The final sequence was confirmed by DNA sequencing (Australian Genome Research Facility, Adelaide, Australia).

Protein expression and purification of SyoA and GcoA

The pET3a vectors containing *syoA*, $syoA_{EE}$, $syoA_{QT}$ *or* $syoA_{ET}$; the pET26 vector containing the *gcoA* gene; and the pET28a vectors containing $gcoA_{EE}$, $gcoA_{QT}$ *or* $gcoA_{ET}$ were transformed into *Escherichia coli* BL21 (DE3) competent cells. The cells were plated on lysogeny broth (LB) agar containing ampicillin (100 μg/ml) for the pET3a vectors and kanamycin (50 μg/ml) for the pET26 and pET28a vectors and incubated at 37 °C overnight (~16–20 h). Single colonies were used to inoculate a 50 mL LB starter culture containing the appropriate antibiotic and grown overnight (~16–20 h) at 37 °C with shaking (180 rpm). 2.5 L flasks containing 1 L LB with antibiotics were inoculated with 1:100 v/v starter culture and incubated, 37 °C with shaking (150 rpm). At an OD_{600} of 2, 1% v/v ethanol and 0.02% v/v benzyl alcohol were added to induce chaperone expression[51], and the cultures incubated at 18 °C with shaking 100 rpm. Additionally, 3 mL/L trace elements (Per liter: Na_2EDTA (20.1 g), $FeCl_3.6H_2O$ (16.7 g), $CaCl_2.H_2O$ (0.74 g), $CoCl_2.6H_2O$ (0.25 g), $ZnSO_4.7H_2O$ (0.18 g), $MnSO_4.4H_2O$ (0.132 g), $CuSO_4.5H_2O$ (0.10 g)) were added for cofactor incorporation. After 30 min, protein expression was induced with addition of IPTG (isopropyl β-D-1-thiogalactopyranoside) to a final concentration of 0.1 mM, and the culture incubated overnight ~20 h at 18 °C with shaking at 100 rpm. Cells were harvested by centrifugation (6200 × *g*, 15 min, 4 °C).

The cell pellet was resuspended in ice-cold lysis buffer (50 mM Tris, pH 7.5, 50 mM NaCl, 20 mM imidazole). Cells were lysed by sonication (30 cycles of 15 s on, 45 s off, 70% amplitude, 19 mm probe, Sonics Vibra-Cell) and cell lysate clarified by centrifugation (40,000 × *g*, 20 min, 4 °C). Proteins were purified by immobilized nickel affinity chromatography (HisTrap HP, 5 mL column Cytiva) using a linear gradient of 20–250 mM imidazole at a flow rate of 5 mL/min. The samples were buffer exchanged into 50 mM Tris, pH 7.5 by centrifugal ultrafiltration using a Vivaspin 20 centrifugal concentrator (Sartorius) with a 10 kDa molecular weight cut-off. Wild type SyoA and GcoA were further purified by anion exchange (HiTrap Q FF, 5 mL Cytiva) using a linear gradient of 0–500 mM NaCl at a flow rate of 5 mL/min. Purified protein was concentrated by ultrafiltration to <10 mL and stored in 40–50% v/v glycerol at −20 °C. Glycerol was removed before use using a PD-10 desalting column (Cytiva) equilibrated in 50 mM Tris, pH 7.5. The concentration of each protein was estimated using the following extinction coefficients: SyoA (ε_{417nm} = 123 mM^{-1} cm^{-1})[4], GcoA (ε_{417nm} = 119 mM^{-1} cm^{-1})[4].

Protein expression and purification of SyoB and GcoB

The pET29b vectors containing *syoB* or *gcoB* were transformed into *Escherichia coli* BL21 (DE3) competent cells. The cells were plated on LB agar containing kanamycin (50 μg/ml) and incubated at 37 °C overnight (~16–20 h). Cells were grown as described above in 2.5 L flasks containing 1 L LB with antibiotics. At an OD_{600} of 0.6, 1% v/v ethanol and 0.02% v/v benzyl alcohol were added and the cultures incubated at 18 °C with shaking 80 rpm. Additionally, 1 mM L-cysteine and 0.5 mM ferric ammonium citrate were added to aid cofactor incorporation. After 30 min, protein expression was induced with addition of 0.1 mM IPTG, and the culture incubated overnight ~20 h at 20 °C with shaking at 80 rpm. Cells were harvested by centrifugation (6200 × *g*, 15 min, 4 °C).

The cell pellet was resuspended in ice-cold lysis buffer (50 mM Tris, pH 7.5, 500 mM NaCl, 20 mM imidazole, 1 mM DTT) for SyoB and (50 mM Tris, pH 7.5, 50 mM NaCl, 1 mM DTT) for GcoB. Cells were lysed by sonication (30 cycles of 15 s on, 45 s off, 70% amplitude, 19 mm probe, Sonics Vibra-Cell) and cell lysate clarified by centrifugation (40,000 × *g*, 20 min, 4 °C). SyoB was purified by immobilized nickel affinity chromatography (HisTrap HP, 5 mL column Cytiva) using a linear gradient of 20–250 mM imidazole at a flow rate of 5 mL/min. GcoB was purified by ion-exchange chromatography, using a DEAE Sepharose column and characterized by UV-Vis absorbance spectroscopy (Supplementary Fig. 9). A linear gradient of 50–500 mM NaCl was used to elute the protein at a flow rate of 5 mL/min. The samples were buffer exchanged into 50 mM Tris, pH 7.5 by centrifugal ultrafiltration using a Vivaspin 20 centrifugal concentrator (Sartorius) with a 10 kDa molecular weight cut-off. Purified protein was concentrated by ultrafiltration to <10 mL and stored in 40–50% v/v glycerol at -20 °C. Glycerol was removed before use using a PD-10 desalting column (Cytiva) equilibrated in 50 mM Tris, pH 7.5. The concentration of SyoB and GcoB were estimated using the extinction coefficient (ε_{423nm} = 25.2 mM^{-1} cm^{-1})[2].

Protein crystallization and structure determination

For crystallization, the N-terminal His_6 tag was cleaved using His_6-TEV protease and separated from His_6-tagged SyoA, His6-tag and TEV protease by IMAC. SyoA was further purified by size exclusion chromatography (HiLoad 16/600 Superdex 200 pg, Cytiva) and concentrated to ~15 mg mL^{-1} in 20 mM Tris pH 7.5 by ultrafiltration. Crystals were grown by sitting drop vapor diffusion at 289 K using 1 μL of protein with 1 μL of reservoir solution, including PEG/Ion I&II, Index, and PGA screens. SyoA in the substrate-free state crystallized within 1 week in conditions comprising 0.25 mM syringol (from a 50 mM stock in DMSO), 0.1 M sodium acetate pH 5, 5% w/v γ-PGA (γ-polyglutamic acid) and 12% w/v PEG 8000. Crystals were cryoprotected in reservoir solution supplemented with 25% v/v glycerol prior to flash cooling in liquid nitrogen. SyoA in the substrate-bound state crystallized within 1 week in conditions comprising 20 mM substrate (from a 200 mM stock in 40% DMSO), 0.2 M magnesium nitrate hexahydrate pH 5.9, 20% w/v PEG 3350 or 0.2 M lithium nitrate pH 7.1, 20% w/v PEG 3350. Crystals were cryoprotected in NVH oil prior to flash cooling in liquid nitrogen.

Diffraction data were collected for the substrate-free and syringol-bound crystals of SyoA at the MX1 beamline at the Australian Synchrotron[52]. Diffraction data were collected remotely for the 4-methylsyringol-bound crystal of SyoA at the MX2 beamline at the Australian Synchrotron using the Blu-Ice GUI interface to EPICS control and qeGUI[53]. 360° of data were collected using 0.1° oscillations at a wavelength of 0.9357 Å at 100 K. The data were autoprocessed, indexed and integrated using xdsme v0.6.6[54] in space group $P2_12_12$ for the substrate-free structure and $P2_1$ for the substrate-bound

structures. Data were scaled and merged using Aimless v0.7.8[55] in CCP4 v8.0[56] and truncated to 1.98 Å, 1.26 Å, and 1.12 Å for the substrate-free, syringol-bound and 4-methylsyringol-bound structures, respectively. Molecular replacement was performed using Phaser-MR v2.7.16[57] with an Alphafold2 v2.3.1[58] model of SyoA made using ColabFold v1.5.1[59] as the initial search model for the substrate-free structure, which was subsequently used to phase the syringol-bound model. The refined syringol-bound structure was then used as the search model to phase the 4-methylsyringol-bound data. The models were refined with Phenix.refine v1.20.1_4487 and built and improved in Coot v0.9.8.3[60] over multiple iterations. Data collection and refinement statistics are summarized in Supplementary Table 1. Molecular graphics, structural alignments and RMSD calculations were performed with UCSF ChimeraX v1.6.1[61].

Substrate binding analysis and dissociation constants

To determine substrate binding, SyoA or GcoA was diluted to ~3 µM in 50 mM Tris pH 7.5 in 500 µL and substrate added in 1 µL aliquots from a 100 mM stock in DMSO. The absorbance was measured between 600–250 nm on a Cary 60 UV-Vis Spectrophotometer (Agilent Technologies) until no further shift was observed.

To determine substrate binding affinity (K_D), SyoA was diluted to ~2–8 µM in 50 mM potassium phosphate buffer pH 7.4 in a volume of 2.5 mL. Aliquots (0.5–5 µL) of 1, 10, or 100 mM substrate stock solutions in DMSO were added using a 5 µL Hamilton syringe. The difference spectrum was recorded from 300–600 nm. Aliquots of substrate were added until no further spectral shift occurred and no more than 10 µL of each stock solution was added to avoid diluting the enzyme. Titrations were performed in triplicate. Binding curve graphing analysis was performed with GraphPad Prism 10. The peak-to-trough absorbance difference, ΔA ($A_{peak} - A_{trough}$), was then plotted against substrate concentration. The ΔA was calculated using $A_{390\text{-}419\ nm}$ for syringol and 4-methylsyringol, $A_{500\text{-}419\ nm}$ for 4-allylsyringol and $A_{500\text{-}570\ nm}$ for syringaldehyde. To obtain the dissociation constant the data were fitted to the hyperbolic (Michaelis-Menten) equation (Equation 1), where K_D denotes the binding constant, [S] the substrate concentration, ΔA the peak-to-trough ratio, and ΔA_{max} the maximum peak-to-trough absorbance.

$$\Delta A = \frac{\Delta A_{\max} \times [S]}{K_D + [S]} \quad (1)$$

In vitro NADH/O_2-driven reactions

In vitro NADH/O_2-driven reactions were performed at 30 °C in a total volume of 600–1200 µL. Reactions were performed in a quartz cuvette (with a 1 cm path length) and contained 1 µM SyoA or 0.5 µM GcoA, 1 µM SyoB or GcoB, and 100 µg mL^{-1} catalase (from bovine liver) in oxygenated Tris buffer (50 mM, pH 7.5). This mixture was used to blank the spectrophotometer. NADH was added to a concentration of ~320 µM and the background rate of NADH air oxidation was measured spectrophotometrically at 340 nm ($\varepsilon 340\ nm = 6.22\ mM^{-1}\ cm^{-1}$). The reaction was initiated by addition of 1 mM substrate (from a 100 mM stock solution in DMSO) and NADH oxidation was monitored at 340 nm for the first ~10 min, and the reactions were then left at room temperature for ~1 h to ensure that the NADH was completely consumed. Control reactions were also performed in which the P450 was omitted from the turnover mixture.

In vitro H_2O_2-driven reactions

In vitro H_2O_2 turnovers were performed at 30 °C in a total volume of 600 µL and contained 1 µM P450, 0.5–2 mM substrate from a 100 mM stock dissolved in DMSO and 10 mM H_2O_2 for the SyoA reactions and 20 mM H_2O_2 for the GcoA reactions in Tris buffer (50 mM, pH 7.5). Each reaction was performed in triplicate. Reactions were incubated for 2 mins at 30 °C prior to addition of H_2O_2 to initiate the reaction (H_2O_2 was added from a 200 mM stock freshly prepared before each experiment from a 30% w/w stock). All reactions were quenched at 60 min with 10 µL of 10 mg mL^{-1} catalase. Control reactions without P450 were performed to assess stability of substrates and products with H_2O_2.

Formaldehyde assay

Formaldehyde production was measured using a colorimetric Purpald assay[62]. To determine the concentration of formaldehyde, 120 µL of the in vitro turnover mixture was mixed with 48 µL of 32 mM Purpald (dissolved in 2 M NaOH) and 432 µL 50 mM Tris, pH 7.5. The reaction was allowed to develop at room temperature by shaking for 60 min. The absorbance at 550 nm was recorded and the concentration of formaldehyde calculated using a calibration curve made with 0–400 µM formaldehyde. Reactions excluding the Purpald reagent were used as a baseline and the concentration of formaldehyde normalized against controls reactions without P450.

Product analysis by HPLC

Analytical High Performance Liquid Chromatography (HPLC) was performed on a Shimadzu LC-20AD equipped with a Phenomenex Kinetex 5 u XB-C18 100 Å column (250 mm×4.6 mm, 5 µM), SIL-20A autosampler, CTO-20A, SPD-20A UV detector, and CBM-20Alite communications module. Each sample and standard were injected at a volume of 20 µL. A gradient of 20–95% MeCN in water (with 0.1% TFA) over 30 min was used to elute the samples at a rate of 1 mL min^{-1} and the eluate was monitored at 254 nm.

To prepare turnover mixtures for HPLC, 132 µL of the in vitro turnover mixture was mixed with 66 µL of MeCN and 2 µL of internal standard (IS, 10 mM 9-hydroxyfluorene in EtOH) and centrifuged at 15,800 × g for 3 mins to remove particulate matter. Calibration curves were constructed to quantify the product where available. Solutions of products with concentrations of 20, 50, 100, 200, and 500 µM were prepared for HPLC analysis in the same way as the turnovers. A plot of product peak area/IS peak area versus product concentration was then constructed.

Product analysis by GC-MS

In vitro H_2O_2 turnovers were performed as described above in 600 µL and analytes extracted once with 300 µL ethyl acetate. Samples were thoroughly mixed for 30 s by vortex. After phase separation, 180 µL of the organic layer was transferred to vials and analyzed by gas chromatography-mass spectrometry (GC-MS) using a Shimadzu GC-2010 equipped with a QP2010S GC-MS detector. 1 µL of sample was injected for analysis using a splitting ratio of 20. Separation of the analytes was done using a DB-5MS UI column (30 mm × 0.25 mm × 0.25 µm) at a flowrate of 1.4 mL min^{-1} and the following temperature settings: Initial temperature of 100 °C held for 2 min, increased to 270 °C at 10 °C min^{-1} and held at 270 °C for 6 min. The injection inlet temperature was 230 °C, ion source temperature 250 °C.

Reporting summary

Further information on research design is available in the Nature Portfolio Reporting Summary linked to this article.

Data availability

The atomic coordinates and structure factors generated in this study have been deposited in the Protein Data Bank under accession codes 8u09 SyoA; 8u19 syringol-bound SyoA, and 8u1i 4-methylsyringol-bound SyoA; structural comparisons were made to 5ncb guaiacol-bound GcoA. Source data including spectrophotometric data, HPLC data, per residue B-factors, RMSD measurements, binding affinity calculations, and absorbance data generated in this study are provided with this paper as a Source Data file. Source data are provided with this paper.

References

1. Wolf, M. E., Hinchen, D. J., DuBois, J. L., McGeehan, J. E. & Eltis, L. D. Cytochromes P450 in the biocatalytic valorization of lignin. *Curr. Opin. Biotechnol.* **73**, 43–50 (2022).
2. Mallinson, S. J. B. et al. A promiscuous cytochrome P450 aromatic *O*-demethylase for lignin bioconversion. *Nat. Commun.* **9**, 2487 (2018).
3. Fetherolf, M. M. et al. Characterization of alkylguaiacol-degrading cytochromes P450 for the biocatalytic valorization of lignin. *Proc. Natl Acad. Sci. USA* **117**, 25771–25778 (2020).
4. Harlington, A. C., Shearwin, K. E., Bell, S. G. & Whelan, F. Efficient *O*-demethylation of lignin monoaromatics using the peroxygenase activity of cytochrome P450 enzymes. *Chem. Commun.* **58**, 13321–13324 (2022).
5. Ralph, J., Lapierre, C. & Boerjan, W. Lignin structure and its engineering. *Curr. Opin. Biotechnol.* **56**, 240–249 (2019).
6. Becker, J. & Wittmann, C. A field of dreams: Lignin valorization into chemicals, materials, fuels, and health-care products. *Biotechnol. Adv.* **37**, 107360 (2019).
7. Abe, T., Masai, E., Miyauchi, K., Katayama, Y. & Fukuda, M. A tetrahydrofolate-dependent *O*-demethylase, LigM, is crucial for catabolism of vanillate and syringate in *Sphingomonas paucimobilis* SYK-6. *J. Bacteriol.* **187**, 2030–2037 (2005).
8. Masai, E. et al. A novel tetrahydrofolate-dependent *O*-demethylase gene is essential for growth of *Sphingomonas paucimobilis* SYK-6 with syringate. *J. Bacteriol.* **186**, 2757–2765 (2004).
9. Perez, J. M. et al. Redundancy in aromatic *O*-demethylation and ring-opening reactions in *Novosphingobium aromaticivorans* and their impact in the metabolism of plant-derived phenolics. *Appl. Environ. Microbiol* **87**, e02794–20 (2021).
10. Notonier, S. et al. Metabolism of syringyl lignin-derived compounds in *Pseudomonas putida* enables convergent production of 2-pyrone-4,6-dicarboxylic acid. *Metab. Eng.* **65**, 111–122 (2021).
11. Machovina, M. M. et al. Enabling microbial syringol conversion through structure-guided protein engineering. *Proc. Natl Acad. Sci. USA* **116**, 13970–13976 (2019).
12. Jiang, Y. et al. Regioselective aromatic *O*-demethylation with an artificial P450BM3 peroxygenase system. *Catal. Sci. Technol.* **10**, 1219–1223 (2020).
13. Guengerich, F. P. Mechanisms of cytochrome P450-catalyzed oxidations. *ACS Catal.* **8**, 10964–10976 (2018).
14. Huang, X. & Groves, J. T. Oxygen activation and radical transformations in heme proteins and metalloporphyrins. *Chem. Rev.* **118**, 2491–2553 (2018).
15. Rittle, J. & Green, M. T. Cytochrome P450 compound I: capture, characterization, and C-H bond activation kinetics. *Science* **330**, 933–937 (2010).
16. Krest, C. M. et al. Reactive intermediates in cytochrome P450 catalysis. *J. Biol. Chem.* **288**, 17074–17081 (2013).
17. Imai, M. et al. Uncoupling of the cytochrome P-450cam monooxygenase reaction by a single mutation, threonine-252 to alanine or valine: A possible role of the hydroxy amino acid in oxygen activation. *Proc. Natl Acad. Sci. USA* **86**, 7823–7827 (1989).
18. Raag, R. et al. Crystal structure of the cytochrome P-450CAM active site mutant Thr252. Ala. *Biochemistry* **30**, 11420–11429 (1991).
19. Kimata, Y., Shimada, H., Hirose, T. & Ishimura, Y. Role of Thr-252 in cytochrome P450cam: a study with unnatural amino acid mutagenesis. *Biochem. Biophys. Res. Commun.* **208**, 96–102 (1995).
20. Vidakovic, M., Sligar, S. G., Li, H. & Poulos, T. L. Understanding the role of the essential Asp251 in cytochrome P450cam using site-directed mutagenesis, crystallography, and kinetic solvent isotope effect. *Biochemistry* **37**, 9211–9219 (1998).
21. Coleman, T. et al. Structural insights into the role of the acid-alcohol pair of residues required for dioxygen activation in cytochrome P450 enzymes. *J. Biol. Inorg. Chem.* **25**, 583–596 (2020).
22. Shoji, O. & Watanabe, Y. Peroxygenase reactions catalyzed by cytochromes P450. *J. Biol. Inorg. Chem.* **19**, 529–539 (2014).
23. Hrycay, E. G. & Bandiera, S. M. "Monooxygenase, peroxidase and peroxygenase properties and reaction mechanisms of cytochrome P450 enzymes" in *Monooxygenase, Peroxidase and Peroxygenase Properties and Mechanisms of Cytochrome P450. Advances in Experimental Medicine and Biology* (eds Hrycay, E. G. & Bandiera, S. M.) 1–61 (Springer, 2015).
24. Albertolle, M. E. & Guengerich, P. F. The relationships between cytochromes P450 and H_2O_2: production, reaction, and inhibition. *J. Inorg. Biochem* **186**, 228–234 (2018).
25. Matsunaga, I., Ueda, A., Fujiwara, N., Sumimoto, T. & Ichihara, K. Characterization of the ybdT gene product of *Bacillus subtilis*: novel fatty acid β-hydroxylating cytochrome P450. *Lipids* **34**, 841–846 (1999).
26. Belcher, J. et al. Structure and biochemical properties of the alkene producing cytochrome P450 OleTJE (CYP152l1) from the *Jeotgalicoccus* sp. 8456 bacterium. *J. Biol. Chem.* **289**, 6535–6550 (2014).
27. Munro, A. W., McLean, K. J., Grant, J. L. & Makris, T. M. Structure and function of the cytochrome P450 peroxygenase enzymes. *Biochem. Soc. Trans.* **46**, 183–196 (2018).
28. Ebrecht, A. C., Smit, M. S. & Opperman, D. J. Natural alternative heme-environments allow efficient peroxygenase activity by cytochrome P450 monooxygenases. *Catal. Sci. Technol.* **13**, 6264–6273 (2023).
29. Hofrichter, M., Kellner, H., Pecyna, M. J. & Ullrich, R. Fungal unspecific peroxygenases: heme-thiolate proteins that combine peroxidase and cytochrome P450 properties. *Adv. Exp. Med. Biol.* **851**, 341–368 (2015).
30. Correll, C. C., Batie, C. J., Ballou, D. P. & Ludwig, M. L. Phthalate dioxygenase reductase: a modular structure for electron transfer from pyridine nucleotides to [2Fe-2S]. *Science* **258**, 1604–1610 (1992).
31. Dakin, H. D. The oxidation of hydroxy derivatives of benzaldehyde, acetophenone and related substances. *Am. Chem. J.* **42**, 477–498 (1909).
32. Nagano, S. & Poulos, T. L. Crystallographic study on the dioxygen complex of wild-type and mutant cytochrome P450cam. Implications for the dioxygen activation mechanism. *J. Biol. Chem.* **280**, 31659–31663 (2005).
33. Harth, F. M. et al. Selective demethylation reactions of biomass-derived aromatic ether polymers for bio-based lignin chemicals. *Green. Chem.* **25**, 10117–10143 (2023).
34. Winkler, C. K., Schrittwieser, J. H. & Kroutil, W. Power of biocatalysis for organic synthesis. *ACS Cent. Sci.* **7**, 55–71 (2021).
35. Zhou, N., Thilakarathna, W. W., He, Q. S. & Rupasinghe, H. V. A review: depolymerization of lignin to generate high-value bio-products: opportunities, challenges, and prospects. *Front. Energy Res.* **9**, 758744 (2022).
36. Lee, S., Kang, M., Bae, J. H., Sohn, J. H. & Sung, B. H. Bacterial valorization of lignin: strains, enzymes, conversion pathways, biosensors, and perspectives. *Front. Bioeng. Biotechnol.* **7**, 209 (2019).
37. Lu, X. & Gu, X. A review on lignin pyrolysis: pyrolytic behavior, mechanism, and relevant upgrading for improving process efficiency. *Biotechnol. Biofuels Bioprod.* **15**, 106 (2022).
38. Lee, Y. T., Wilson, R. F., Rupniewski, I. & Goodin, D. B. P450cam visits an open conformation in the absence of substrate. *Biochem* **49**, 3412–3419 (2010).
39. Santos, S. F. G., Bommareddy, R. R., Black, G. W., Singh, W. & Huang, M. The substrate specificity in the *O*-demethylation of 4-alkylguaiacols by cytochrome P450 AgcAP450. *Catal. Sci. Technol.* **13**, 2070–2079 (2023).
40. Hall, E. A., Sarkar, M. R. & Bell, S. G. The selective oxidation of substituted aromatic hydrocarbons and the observation of

uncoupling via redox cycling during naphthalene oxidation by the CYP101B1 system. *Catal. Sci. Technol.* **7**, 1537–1548 (2017).
41. Zhao, L. et al. Biological degradation of lignin: a critical review on progress and perspectives. *Ind., Crop. Prod.* **188**, 115715 (2022).
42. Erickson, E. et al. Critical enzyme reactions in aromatic catabolism for microbial lignin conversion. *Nat. Catal.* **5**, 86–98 (2022).
43. Sun, S. et al. Lytic polysaccharide monooxygenase synergized with lignin-degrading enzymes for efficient lignin degradation. *iScience* **26**, 107870 (2023).
44. Lahtinen, M., Kruus, K., Heinonen, P. & Sipilä, J. On the reactions of two fungal laccases differing in their redox potential with lignin model compounds: products and their rate of formation. *J. Agric. Food Chem.* **57**, 8357–8365 (2009).
45. Kim, J., Nguyen, T. V. T., Kim, Y. H., Hollmann, F. & Park, C. B. Lignin as a multifunctional photocatalyst for solar-powered biocatalytic oxyfunctionalization of C–H bonds. *Nat. Synth.* **1**, 217–226 (2022).
46. Kommedal, E. G. et al. Visible light-exposed lignin facilitates cellulose solubilization by lytic polysaccharide monooxygenases. *Nat. Commun.* **14**, 1063 (2023).
47. Li, F. et al. Microbial lignin valorization through depolymerization to aromatics conversion. *Trends Biotechnol.* **40**, 1469–1487 (2022).
48. Gee, A. R. et al. Efficient biocatalytic C–H bond oxidation: an engineered heme-thiolate peroxygenase from a thermostable cytochrome P450. *Chem. Commun.* **59**, 13486–13489 (2023).
49. Podgorski, M. N. et al. Engineering peroxygenase activity into cytochrome P450 monooxygenases through modification of the oxygen binding region. *ACS Catal.* **14**, 7426–7443 (2024).
50. Gibson, D. G. et al. Enzymatic assembly of DNA molecules up to several hundred kilobases. *Nat. Methods* **6**, 343–345 (2009).
51. De Marco, A., Vigh, L., Diamant, S. & Goloubinoff, P. Native folding of aggregation-prone recombinant proteins in *Escherichia coli* by osmolytes, plasmid- or benzyl alcohol-overexpressed molecular chaperones. *Cell Stress Chaperones* **10**, 329–339 (2005).
52. Cowieson, N. P. et al. MX1: a bending-magnet crystallography beamline serving both chemical and macromolecular crystallography communities at the Australian Synchrotron. *J. Synchrotron Radiat.* **22**, 187–190 (2015).
53. Aragão, D. et al. MX2: a high-flux undulator microfocus beamline serving both the chemical and macromolecular crystallography communities at the Australian Synchrotron. *J. Synchrotron Radiat.* **25**, 885–891 (2018).
54. Legrand, P. XDSME: XDS made easier. GitHub repository. accessed 16 January 2024. Available at: https://github.com/legrandp/xdsme (2017).
55. Evans, P. R. & Murshudov, G. N. How good are my data and what is the resolution? *Acta Crystallogr. D. Biol. Crystallogr.* **69**, 1204–1214 (2013).
56. Agirre, J. et al. The CCP4 suite: integrative software for macromolecular crystallography. *Acta Crystallogr. D. Struct. Biol.* **79**, 449–461 (2023).
57. McCoy, A. J. et al. Phaser crystallographic software. *J. Appl. Crystallogr.* **40**, 658–674 (2007).
58. Jumper, J. et al. Highly accurate protein structure prediction with AlphaFold. *Nature* **596**, 583–589 (2021).
59. Mirdita, M. et al. ColabFold: making protein folding accessible to all. *Nat. Methods* **19**, 679–682 (2022).
60. Emsley, P., Lohkamp, B., Scott, W. G. & Cowtan, K. Features and development of Coot. *Acta Crystallogr. D. Biol. Crystallogr.* **66**, 486–501 (2010).
61. Meng, E. C. et al. UCSF ChimeraX: tools for structure building and analysis. *Prot. Sci.* **32**, 4792 (2023).
62. Quesenberry, M. S. & Lee, Y. C. A rapid formaldehyde assay using purpald reagent: application under periodation conditions. *Anal. Biochem.* **234**, 50–55 (1996).

Acknowledgements

This work was funded, in part, through Australian Research Council grants DP200102411 (to S.G.B. and others) and DP230103062 (to F.W. and K.E.S.). This research was undertaken on the MX1 and MX2 beamlines at the Australian Synchrotron, part of Australian Nuclear Science and Technology Organization, and made use of the ACRF detector on MX2. We acknowledge financial support from the Australian Synchrotron to use this facility. A.C.H. was supported by Wine Australia, with levies from Australia's grapegrowers and winemakers and matching funds from the Australian Government. A.C.H. and T.D. were supported by Research Training Program (RTP) scholarships from the Australian government. F.W. was supported by the Ramsay Fellowship in Applied Science and Microscopy Australia (ROR: 042mm0k03). We acknowledge that this research was conducted on the traditional Country of the Kaurna people and the Boonwurrung/Bunurong and Wurundjeri people of the Kulin Nation and pay our respects to Elders past and present.

Author contributions

A.C.H., T.D., K.E.S., S.G.B., and F.W. designed research; A.C.H., T.D., K.E.S., S.G.B., and F.W. performed research; A.C.H., T.D., S.G.B., and F.W. analyzed data; A.C.H., K.E.S., S.G.B., and F.W. wrote the paper.

Competing interests

The authors declare no competing interests.

Additional information

Supplementary information The online version contains supplementary material available at https://doi.org/10.1038/s41467-025-57129-6.

Correspondence and requests for materials should be addressed to Stephen G. Bell or Fiona Whelan.

Peer review information *Nature Communications* thanks Jing-Ke Weng and the other anonymous reviewer(s) for their contribution to the peer review of this work. A peer review file is available.